List of Symbols

σ_{ij}	local stress tensor
σ	maximum local normal stress
σ_c	critical local normal stress
Σ_{ij}	global stress tensor
s_{ij}	global deviatoric stress tensor
Σ	global maximum tensile stress
Σ_c	critical global tensile stress
Σ^{vM}	global von Mises stress
Σ^H	global hydrostatic stress
T	triaxiality
L	Lode parameter
k	geometric factor depending on the particle shape
E_p	tangent modulus of the plastically deforming matrix
ϵ_{ij}	strain tensor
$\dot{\epsilon}_{ij}$	strain rate tensor
ϵ^e_{ij}	elastic strain tensor
ϵ^p_{ij}	plastic strain tensor
ϵ^p	equivalent plastic strain
$\dot{\epsilon}^p$	equivalent plastic strain rate
S_{ijkl}	compliance tensor
κ	stress concentration factor
κ^p	plastic stress concentration factor
κ^e	elastic stress concentration factor
$\dot{f}_g$	rate of void volume fraction increase due to growth
$\dot{f}_n$	rate of void volume fraction increase due to nucleation of voids
f_N	volume fraction of particles at which voids can nucleate
v	driving force for nucleation
ω_{ij}	strain angle with respect to i and j components
ϕ_{ij}	stress angle with respect to i and j components

Criterion for void nucleation by particle debonding in metals obtained from molecular dynamics simulations

Qian Qian Zhao*, Ryan B. Sills

Department of Materials Science and Engineering, Rutgers University, Piscataway, NJ 08854, USA.

Abstract

The critical conditions for void nucleation by particle debonding at a θ-particle in an aluminum matrix are identified through a comprehensive set of molecular dynamics simulations spanning a range of stress triaxialities and Lode parameter values. Specifically, it is determined that nucleation occurs when the local normal stress at the matrix-particle interface reaches a critical value of 8.14 GPa. When plasticity occurs in the matrix prior to nucleation, an additional plastic stress concentration is observed as a result of the plastic strain build up around the particle. Our results indicate that this plastic stress concentration factor increases roughly linearly with equivalent plastic strain, independent of triaxiality and Lode parameter. Comparing our results with the literature, we observe a much stronger influence of plastic strain than is predicted by continuum plasticity theory. We argue that this difference derives from the fact that nucleation is fundamentally driven by local stress hot spots resulting from the heterogeneity of plastic strain, while continuum theory is based on homogenized plastic strain fields. These results provide guidance for development of ductile fracture engineering models, while giving a warning regarding the use of continuum theory to predict damage initiation phenomena in metals.

---

*Corresponding author

Email addresses: `qz161@rutgers.edu` (Qian Qian Zhao), `ryan.sills@rutgers.edu` (Ryan B. Sills)

Preprint submitted to Elsevier *December 5, 2024*

1. Introduction

Ductile fracture of metals results from the nucleation, growth, and coalescence of voids [1]. Void nucleation—the first step which initiates this process—commonly occurs at second phase particles, either via cracking or debonding of the particles (although nucleation at other sites such as grain boundaries is also observed) [2]. Our focus here is on void nucleation by particle debonding. The void nucleation process has been studied thoroughly using continuum models, such as elastic-plastic and cohesive surface finite element modeling [3, 4, 5, 6]. A major focus of this research has been on the critical conditions associated with nucleation. Nucleation models have been developed assuming that nucleation occurs when either a critical energy [7], stress state [8], or strain state [9] is reached. Recently, Noell et al. [2] argued that of these approaches the most appropriate is a model based on reaching a local critical stress state, subject to the constraint that nucleation must be energetically favorable (e.g., free energy decreases as a result of nucleation). However, to our knowledge, no prior research has evaluated the critical conditions of nucleation using a model which accounts for the influence of discrete defects (e.g., dislocations) and discrete plastic slip events, since most prior work is based on continuum models. The goal of this work is to use molecular dynamics (MD) simulations to determine the critical conditions for void nucleation via particle debonding, so that the influence of local defects and slip events can be captured and understood.

For stress-based nucleation criteria, which are the focus here, the main challenge is to establish a condition relating the globally applied (volume-averaged) stress state, Σ_{ij}, to the local stress state at the particle interface, σ_{ij}, at the onset of void nucleation. Noell et al. argue that the local tensile stress normal to the particle interface, σ, is the main driving force for void nucleation by particle debonding. Hence, we may write a stress-based nucleation criterion in the form: $\sigma_c = f(\Sigma_{ij}, ...)$, where σ_c is the critical local normal stress and ... denotes other possible factors affecting void nucleation such as plastic strain and particle shape. In this framing, Argon et al. [8] proposed a criterion of the form:

$$\sigma_c = \Sigma^{vM} + \Sigma^{H} \tag{1}$$

where Σ^{vM} and Σ^{H} are the global von Mises and hydrostratic stresses, respectively. According to Eq. (1), both the shear (von Mises) and hydrostatic stresses act to drive crack nucleation in equal proportion. However by performing and analyzing cohesive zone simulations of interfacial fracture, Needleman [3] found that the hydrostatic stress contributed less significantly to nucleation. Needleman proposed extending the condition of Argon et al. to the form:

$$\sigma_c = \Sigma^{vM} + c\Sigma^H \tag{2}$$

with $c \approx 0.35$ was obtained for a periodic arrangement of spherical particles debonding axisymmetrically [3]. Subsequently, Shabrov and Needleman [4] considered the case of random particle distributions using square cylinder particles, finding that the constant c was sensitive to particle shape and the degree of particle clustering. Simulations of void nucleation in random particle distributions have since been extended to 3D by Segurado and Llorca [10], Williams et al. [11], and Shakoor et al. [6].

Notably, both of the nucleation criteria given above are independent of the state of plastic strain (although plastic strain is implicitly captured since the flow stress Σ^{vm} depends on it), whereas plastic strain is expected to affect the local stress state surrounding each particle. Beremin [12, 2] derived an approximate solution using Eshelby theory for the stress around an elastic particle embedded in a plastically deforming matrix, obtaining the condition for nucleation:

$$\sigma_c = \Sigma + kE_p\epsilon^p \tag{3}$$

where Σ is the global maximum tensile stress (1st principal stress), k is a geometric factor depending on the particle shape, E_p is the tangent modulus of the plastically deforming matrix, and ϵ^p is the equivalent plastic strain around the particle. Hence, Eq. (3) predicts that the driving force for crack nucleation is linearly dependent on the plastic strain. While Beremin's analysis was approximate, Lee and Mear [13] performed a comprehensive set of numerical calculations to determine the stress state surrounding an elastic spheroidal particle in an elastic-plastic matrix, assessing the influence of stress triaxiality, particle shape (aspect ratio), modulus mismatch between matrix and particle, and the matrix hardening exponent. Their results are framed in terms of the stress concentration factor κ relating the global maximum tensile stress Σ to the maximum local normal stress σ:

$$\kappa = \frac{\sigma}{\Sigma}. \tag{4}$$

Their results indicate that the stress concentration factor evolves with plastic strain, typically increasing up to a saturation value attained around $\epsilon^p \approx 5\%$.

According to these results, we may write the condition for nucleation as

$$\sigma_c = \kappa(\epsilon^p, ...)\Sigma \tag{5}$$

where $\kappa(\epsilon^p, ...)$ is sensitive to ϵ^p and other parameters considered by Lee and Mear [2]. In a similar vein, Charles et al. [14] extended the approach of Needleman [3] by employing a cohesive zone model for interfacial fracture with an interfacial strength that decreased upon accumulation of local plastic strain. The arguments underlying their model were that (1) energy stored in the dislocation structure would be released as a result of interfacial fracture and (2) local dislocation pile ups would concentrate stress at the interface. While powerful, we show below that the results of Lee and Mear are problematic because they are derived from continuum theory where the plastic strain distribution is spatially homogenized. Finally, we note that while the influence of stress triaxiality on void nucleation has been explored in numerous works [3, 13, 4, 15], the influence of the Lode parameter (defined below) has not been considered much [2].

A primary motivator for understanding the criterion for void nucleation is the need to model ductile fracture at the continuum scale [5]. The most widespread model for ductile fracture via void nucleation and coalescence is that of Gurson, Tvergaard, and Needleman (GTN) [16, 17], which treats plasticity in a porous solid with void volume fraction f. The void volume fraction evolves according to the ordinary differential equation

$$\dot{f} = \dot{f}_g + \dot{f}_n, \tag{6}$$

where $\dot{f}_g$ and $\dot{f}_n$ account for the rate of void volume fraction increase due to growth and nucleation of voids, respectively. The void growth term follows straightforwardly from the fact that plastic deformation is isochoric in nature [2]. Void growth in elastic-plastic solids has been studied using finite element simulations and shown to compare well with predictions of the GTN model [18, 19]. However, the void nucleation term $\dot{f}_n$ is on much less firm theoretical footing. The most commonly employed models take the form [5, 2]

$$\dot{f}_n = A_n(v)\dot{\epsilon}^p \tag{7}$$

where $\dot{\epsilon}^p$ is the equivalent plastic strain rate and $A_n(v)$ is the nucleation rate factor with nucleation driving force v. While both stress and strain driving forces have been proposed, the most common approach by far is to assume that plastic strain drives void nucleation: $v = \epsilon^p$ [5, 2]. This is at odds with the idea that void nucleation is fundamentally stress driven [2]. Furthermore, these nucleation rate formulations are not derived from the atomic mechanisms of void nucleation, but rather are phenomenological in nature. A more solid understanding of the atomic mechanisms of void nucleation could help to resolve these issue, and lead towards more micromechanistic continuum models for void nucleation.

The goal of this study is to determine a void nucleation criterion on the basis of MD simulations where discrete defects and slip events are naturally captured. This study builds on our prior work on void nucleation via particle debonding where we employed pure hydrostatic loading [20]. In that study the main focus was on the rate of crack growth *after* a crack had nucleated at the particle interface. In contrast, our goal here is to determine the conditions at which an interface crack nucleates—thereby initiating void nucleation—under a wide range of stress states. Our findings demonstrate the value of Eq. (5) as a void nucleation criterion, while also showing the dangers of using continuum theory to study damage initiation in plastically deforming solids where deformation mechanisms (dislocation slip) are fundamentally heterogeneous.

2. Materials and methods

2.1. Simulation setup

The present study is focused on void nucleation by delamination of spherical θ particles (Al_2Cu) in a face-centered cubic (FCC) Al matrix. Al_2Cu is the stable intermetallic phase of the Al-Cu system that is commonly found in Al-Cu alloys (e.g., 2xxx series) [21]. It has a body-centered tetragonal C16 crystal structure which is incoherent with the Al matrix. Note that in real alloys, these precipitates typically adopt a plate-like geometry, but for simplicity here we use spherical particles. Hence, our results here are likely not quantitatively accurate for Al-Cu alloys, but are expected to be correct within a numerical factor that is dependent on particle shape (which should be explored in future work). We choose this system because of the engineering significance of Al-Cu alloys, and because θ particles have been associated with void nucleation [22]. Other than the inserted θ precipitate, no other defects were initially present in the system (e.g., no dislocations and/or point defects).

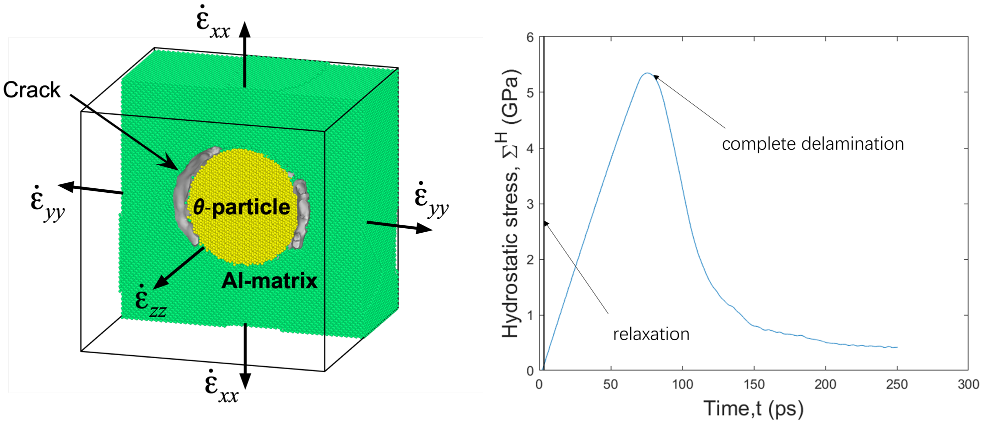

(a) (b)

Figure 1: Simulation details. (a) Snapshot showing periodic simulation cell with a spherical θ-particle with strain rates applied. (b) Time-history of hydrostatic stress Σ^H from a sample with strain angles $\omega_{xy} = \omega_{zx} = 1°$ and with simulation stages marked.

We studied void nucleation using MD simulations [23] in LAMMPS [24]. In MD, classical equations of motion (e.g., Newton's 2nd law) are time integrated to evolve a collection of atoms in time. Forces between the atoms are dictated by the chosen interatomic potential function, which is material-dependent. We utilized the Al-Cu angular-dependent interatomic potential of Apostol and Mishin [25] because of its ability to accurately reproduce the crystal structures and elastic constants of Al and Al_2Cu. When employing an "NVT ensemble", a thermostat controls the temperature of the atoms by adjusting their kinetic energies while the strain state in the system is controlled by adjusting the size and shape of the simulation cell. In our simulations, periodic boundary conditions are employed in all directions by translationally replicating the simulation cell. The initial simulation geometry is shown in Figure 1(a), comprised of a 202.75 Å cubic simulation cell containing a spherical θ particle of radius $R = 50$ Å. All simulations were performed at a temperature of 1 K to avoid thermal activation. In this way, our study here is an assessment of the critical conditions for nucleation without any aid from thermal activation.

Our goal here is to assess the micromechanics of void nucleation under a range of loading conditions. To accomplish this, we employed an NVT ensemble while applying fixed normal strain rates $\dot{\epsilon}_{xx}$, $\dot{\epsilon}_{yy}$, and $\dot{\epsilon}_{zz}$ along each respective coordinate direction. By varying the relative values of the strain rates, a broad range of stress states can be attained. To systematically probe loading space, we introduce two *strain angles* as

$$\omega_{xy} = \tan^{-1}\left(\frac{\dot{\epsilon}_{xx}}{\dot{\epsilon}_{yy}}\right), \qquad \omega_{zx} = \tan^{-1}\left(\frac{\dot{\epsilon}_{zz}}{\dot{\epsilon}_{xx}}\right) \tag{8}$$

which quantify the relative loading rates (similar to Needleman's boundary conditions [3]). We then sampled the full strain angle space by performing simulations in 15° increments from 1 to 360° for both angles, as shown in Figure 2 where "x" markers denote simulation conditions. These strain angles specify the relative strain rates but not the absolute strain rates. To specify the strain rate values, we enforce that the largest strain rate magnitude among $\dot{\epsilon}_{xx}$, $\dot{\epsilon}_{yy}$, and $\dot{\epsilon}_{zz}$ is 5×10^{10} s^{-1}; this strain rate was chosen to minimize artifacts due to a high loading rate, while keeping computational time within reason. The other strain rates are then implied by the associated strain angles. Figure 2 shows the set of strain rate conditions across strain angle space. Note that not all strain angle combinations are permissible, since some require inconsistent signs (e.g., $\omega_{zx} = 0$ means $\dot{\epsilon}_{xx} > 0$ so that only $0 < \omega_{xy} < 180°$ is admissible). This results in a total of 312 MD simulations which are reported in this study. Each simulation contained about 500,000 atoms and ran for about 4 days using 10 CPUs.

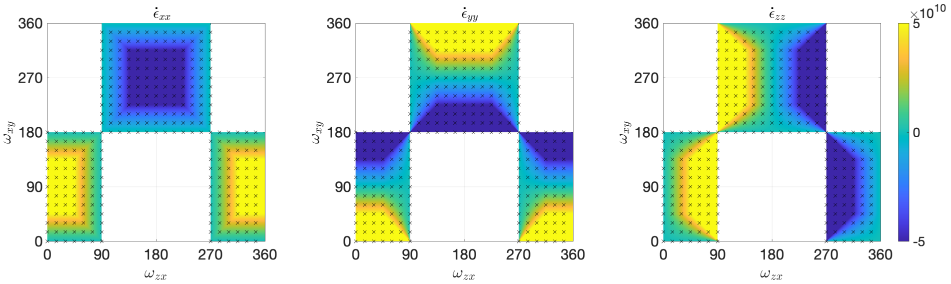

Figure 2: Strain rate loading conditions used in this work, showing color map of strain rates in units of s^{-1} as a function of strain angles ω_{xy} and ω_{zx} with "x" markers denoting conditions where simulations were performed.

Figure 1(b) shows an example hydrostatic stress-time history from a simulation with $\omega_{xy} = 1°$ and $\omega_{zx} = 1°$. Prior to loading, the system is relaxed with an NPT ensemble under zero-stress for 2 ps. Loading is then applied with an NVT ensemble. The stress peaks around the time where the particle completely debonds from the matrix. All the simulations used a thermostat damping parameter value of 0.01 ps, a barostat damping parameter value of 1 ps, and a time step size of 0.001 ps. Each simulation had a maximum duration of 0.25 ns.

2.2. Analysis methods

Simulations were analyzed in numerous ways using LAMMPS, OVITO Pro [26], and MATLAB. In our simulations we observed both crack and dislocation nucleation events. To detect those events, we used common neighbor analysis (CNA) [27] and Voronoi tessellation as follows. Shockley partial dislocations in FCC metals result in the formation of stacking faults, and atoms in these stacking faults exhibit local hexagonal close-packed (HCP) structure. Hence, when dislocations nucleate the number of atoms with HCP structure increases precipitously. In other words, by monitoring the number of HCP atoms we can detect dislocation nucleation events. Specifically, we use a threshold value of 40 HCP atoms to determine when dislocation nucleation occurs, since some spurious identification of HCP atoms occurs throughout the simulation (CNA sometimes assigns incorrect structure type). To detect crack nucleation, we use the local atomic volume determined through Voronoi analysis. At a temperature of 1 K, the atomic volume of FCC Al is around 23 Å^3. When a crack nucleates, the atomic volume begins increasing for atoms adjacent to the crack. Again, by checking when the maximum atomic volume in the simulation cell exceeds a threshold value, we can determine when crack nucleation occurs. Based on trial and error, we determined a suitable threshold value is 28 Å^3. Crack nucleation is deemed to occur at the simulation time where this threshold is exceeded for the remainder of the simulation (in some cases the volume briefly increases but then drops back below the threshold). However, we noticed that in some cases vacancy-like defects with volumes greater than 28 Å^3 can form in the bulk away from the particle's surface as a result of dislocation activity. These defects do not lead to crack nucleation, and hence should be ignored in our analysis. In all simulations, void nucleation by particle debonding was observed (no particle cracking). Accordingly, we only check atoms within 10 Å of the particle's surface (all cracks were observed to nucleate at the particle surface). Finally, in some cases we also quantified the total dislocation density. This was done by extracting all dislocation lines using the dislocation extraction algorithm [28] in OVITO, and then summing the total line length.

To quantify the conditions at which crack and dislocation nucleation occurred, we analyzed the stress and strain state of the system. We primarily focused on the global stresses in our atomistic systems. Local stresses in atomic systems are not thermodynamically well-defined, and hence cannot be quantified unambiguously [29]. The global stresses can be easily determined using the virial stress, as computed by LAMMPS [30]. Given the global stress state Σ_{ij}, we computed the hydrostatic stress and and von Mises stresses as

$$\Sigma^{H} = \Sigma_{kk}/3, \qquad \Sigma^{vM} = \sqrt{\frac{3}{2} s_{ij} s_{ij}},$$

where $s_{ij} = \Sigma_{ij} - \Sigma^{H}\delta_{ij}$ is the deviatoric strain tensor, δ_{ij} is the Kronecker delta, and repeated indices imply summation. Given these stresses, the triaxiality T and Lode parameter L are computed as:

$$T \equiv \frac{\Sigma^{H}}{\Sigma^{vM}}, \qquad L \equiv -\frac{27}{2}\frac{J_3}{\left(\Sigma^{vM}\right)^3}$$

where $J_3 = \det(s_{ij})$ is the third invariant of the deviatoric stress tensor and $\det(\cdot)$ is the determinant operator. T and L are commonly utilized to characterize the stress state in continuum damage models [2]. T quantifies the significance of hydrostatic loading in comparison to shear loading, with $T \to \infty$ meaning purely hydrostatic tensile loading. L is bounded between -1 and 1, and provides a measure of the nature of the stress state. For example, $L = 1$, 0, and -1 denote, respectively, axisymmetric (biaxial) tension (e.g., $\Sigma_{xx} < \Sigma_{yy} = \Sigma_{zz} > 0$), pure shear (e.g., $\Sigma_{xx} = -\Sigma_{yy}$, $\Sigma_{zz} = 0$), and axisymmetric (biaxial) compression (e.g., $\Sigma_{xx} > \Sigma_{yy} = \Sigma_{zz} < 0$). Note that under our stain-rate-based loading conditions here, T and L may vary during loading if there is any plastic strain accumulation. Below we focus on the values of T and L at the moment of void nucleation.

To investigate the global state of plastic strain in each simulation, we first assumed a linear superposition between elastic and plastic strain, i.e., $\epsilon_{ij} = \epsilon^{e}_{ij} + \epsilon^{p}_{ij}$. The total strain ϵ_{ij} is easily determined using the dimensions of the periodic simulation cell (computed by LAMMPS). To determine the elastic strain, we used Hooke's law $\epsilon^{e}_{ij} = S_{ijkl}\Sigma_{kl}$ where S_{ijkl} is the compliance tensor of the composite matrix-particle system. The components of the compliance tensor were computed at 0 K by LAMMPS using standard methods [23]; the results are given in Table 1. Finally, the plastic strain tensor can be estimated as

$$\epsilon^{p}_{ij} = \epsilon_{ij} - S_{ijkl}\Sigma_{kl}. \tag{9}$$

	Al	θ	Composite
S_{11}	0.014	0.007	0.0135
S_{22}	0.014	0.007	0.0135
S_{33}	0.014	0.008	0.0137
S_{44}	0.032	0.034	0.0293
S_{55}	0.032	0.034	0.0290
S_{66}	0.032	0.021	0.0314
S_{12}	-0.005	-0.002	0.0135
S_{13}	-0.005	-0.002	-0.005
S_{23}	-0.005	-0.002	-0.005

Table 1: Elastic constants (units of 1/GPa) for the utilized interatomic potential with pure Al [31], pure θ [25], and the composite Al matrix with θ-particle (computed by the authors). Only showing values with magnitudes greater than 10^{-3}.

We find with this approach that small, non-zero plastic strains of 1% or less may result prior to dislocation nucleation because of nonlinear elastic deformations. Again, since our goal is to compare our results with commonly utilized damage mechanics models, we focus on the equivalent plastic strain, computed as

$$\epsilon^p = \sqrt{\frac{2}{3}\epsilon^p_{ij}\epsilon^p_{ij}}. \tag{10}$$

Finally, for a qualitative analysis, it is useful to also look at the local stress and strain fields. To estimate the local stress, we compute the compute the per-atom Virial stresses in LAMMPS using the Voronoi volume for each atom. These stresses vary significantly from atom to atom, and need to be spatially averaged to yield interpretable results. To determine each atom's local stress state, we average over the stresses for all atoms within a 10 Å radius. To estimate the local plastic strains, we compute the total and elastic strains for each atom using the *Atomic strain* and *Elastic strain calculation* modifiers in OVITO, and then take the difference to get the plastic strain (as in Eq. (9)). These strains are also averaged within a 10 Å neighborhood for each atom to yield smooth fields. Bear in mind that the methods provide semi-quantitative estimates which cannot be interpreted in precise quantitative terms (i.e., the averaging radius is an arbitrary choice).

2.3. Finite element calculations

In order to understand the local stresses around the particle in our simulations, we computed the elastic stress concentration factor associated with each void nucleation event using finite element calculations in Abaqus. For each MD simulation with a void nucleation event, we determined the time of nucleation and then extracted the strain state of the simulation cell 2 ps before nucleation. This strain state was then imposed on a linear elastic finite element system with the same geometry as MD. We used full anisotropic elasticity for the Al and Al_2Cu, using the elastic constants given in Table 1. The elastic stress concentration factor was then found using the following equation:

$$\kappa^e = \frac{\max_{\mathbf{x}}(\sigma)}{\Sigma} \tag{11}$$

where $\max_{\mathbf{x}}(\sigma)$ is the maximum local normal stress at the particle's surface. We also performed a mesh convergence study to determine that our uncertainties for these calculations are less than 2%.

3. Results

3.1. Crack vs. dislocation nucleation process

In our simulations, two distinct defect nucleation events were observed. Crack nucleation, which initiates the void nucleation process, was always observed to occur at the matrix-particle interface (although crack nucleation did not occur in all simulations). This indicates void nucleation via the classical particle debonding mechanism. After nucleating, this crack grew along the interface until total delamination or fracture of the system. This same behavior was observed in our prior work where we utilized pure hydrostatic loading [20], and here is generalized to a broad range of loading conditions. Dislocation nucleation was also observed to occur at the matrix-particle interface with the formation of a Shockley-Read partial dislocations.

Similar to our prior work, in some simulations crack nucleation preceded dislocation nucleation. In these cases, dislocation nucleation subsequently occurred at the tips of the growing interface crack. However, in many simulations dislocation nucleation preceded crack nucleation, which means that the Al matrix deformed plastically prior to crack nucleation. An example of this process is given in Figure 3, where atoms in the θ-particle are colored blue and the remainder of the (empty) box is filled with Al atoms. Atoms

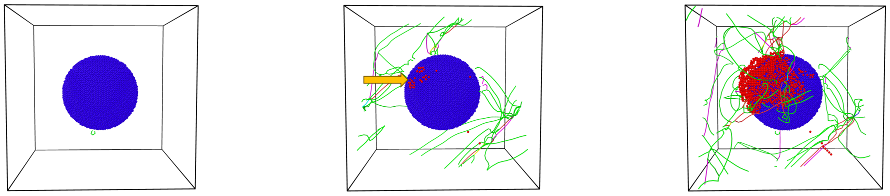

(a) (b) (c)

Figure 3: Simulation snapshots showing behavior when dislocation nucleation precedes crack nucleation, with $\omega_{xy} = 45^\circ$ and $\omega_{zx} = 105^\circ$. (a) Nucleation of a Shockley-Read partial dislocation (green line at particle bottom). (b) After considerable dislocation activity and the appearance of crack nuclei (marked by yellow arrow). (c) After cracks grow in size. Blue atoms are part of the θ particle. Red atoms are associated with cracks. Lines are dislocations (green = Shockley-Read, purple = stair-rod)

associated with cracks (i.e., with atomic volume greater than 28 Å^3) are colored red. Figure 3(a) shows the moment when the first Shockley-Read partial dislocation (green line) nucleates at the particle surface. Over time, the dislocation density increases as more dislocations nucleate and as dislocations bow out and multiply, leading to the dislocation configuration shown in Figure 3(b). Also shown in Figure 3(b) are the crack nucleation sites, denoted by clusters of red atoms marked with a yellow arrow. Figure 3(c) shows the state after the interface crack has grown.

To help clarify the conditions under which these nucleation processes occur, we plot in Figure 4(a) markers to denote different behaviors over the strain angle (ω_{zx} vs. ω_{xy}) space as follows: $\square$ = crack nucleation occurs first, $\bigcirc$ = dislocation nucleation occurs first, $*$ = no cracking was observed (but dislocation nucleation was observed). While clear patterns are observed, they are somewhat difficult to interpret due to the fact that the stress state is not easily deduced from the strain state (e.g., strain angle combination). Accordingly, we also define *stress angles* based on the stress state at which each respective nucleation event occurred as

$$\phi_{xy} = \tan^{-1}\left(\frac{\Sigma_{xx}^{\text{nuc}}}{\Sigma_{yy}^{\text{nuc}}}\right), \qquad \phi_{zx} = \tan^{-1}\left(\frac{\Sigma_{zz}^{\text{nuc}}}{\Sigma_{xx}^{\text{nuc}}}\right) \tag{12}$$

where Σ_{ii}^{nuc} (no sum) denotes the normal stresses at which nucleation occurs. In the case where no cracking was observed, we used the stress at the last time step. In Figure 4(b) we replot the data from Figure 4(a) in stress

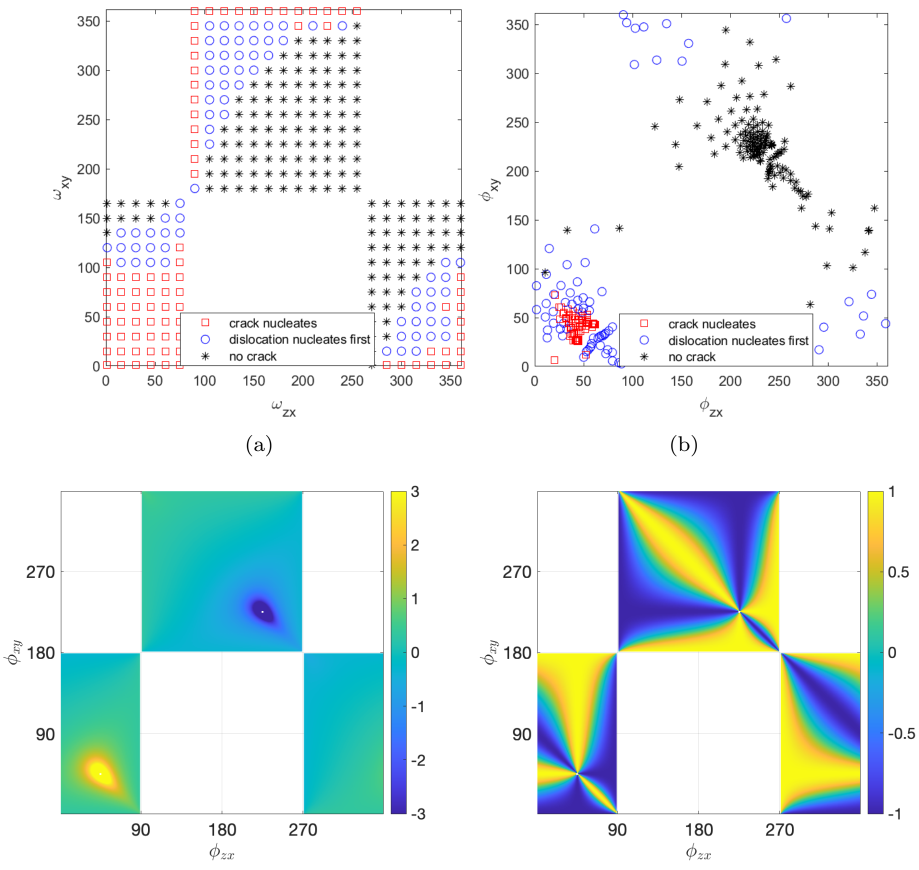

(a)

(b)

(c)

(d)

Figure 4: (a) Strain angle conditions where crack nucleation occurs first (red squares), dislocation nucleation occurs first (blue circles), or no void nucleation occurs (black asterisks). (b) Same results as (a) but using stress angles associated with nucleation. (c) Triaxiality, T, and (d) Lode parameter, L, values as a function of stress angles.

angle space (ϕ_{zx} vs. ϕ_{xy}). For reference, we also plot in Figures 4(c)-(d) the triaxiality T and Lode parameter L associated with these stress angles (these figures assume that shear stresses Σ_{xy}, Σ_{xz}, Σ_{yz} are zero, analysis of our MD stress states confirms that these stress components are negligible in 90% of cases with void nucleation). In Figure 4(b), we now clearly see a meaningful pattern. Crack nucleation occurs first when the system is close to pure hydrostatic tensile loading $\sigma_{xx} = \sigma_{yy} = \sigma_{zz} > 0$ and $T \to \infty$, which is around stress angles of 45°. This is consistent with our prior work, where we found under pure hydrostatic tensile loading that crack nucleation always preceded dislocation nucleation [20]. On the other hand, when the system is loaded in compression in all directions, meaning $\phi_{xy} > 180^\circ$ and $\phi_{zx} > 180^\circ$, no cracking is observed. Under loading conditions between these cases, dislocation nucleation is observed to occur first. There is no clear influence of the Lode parameter L.

To further assess the states of stress associated with crack nucleation events, we replot in Figure 5 the triaxiality T and Lode parameter L values associated with each data point in Figure 4. Figure 5 only shows the triaxiality T and Lode Parameter L at the time of void nucleation. This figure demonstrates that our loading scheme yielded stress states spanning the full range of Lode parameters (-1 to 1) and triaxialities ranging from about 0.5 to 10. Figure 5 also clearly shows that the triaxiality and Lode parameter alone cannot explain the propensity for crack vs. dislocation nucleation. At very high triaxialities $T > 4$, it is clear that crack nucleation is favorable. While it is clear that dislocation nucleation is favored at low triaxialities, there are still many cases with $T < 4$ where crack nucleation occurs first. The propensity for dislocation nucleation seems to slightly increase with increasing Lode parameter.

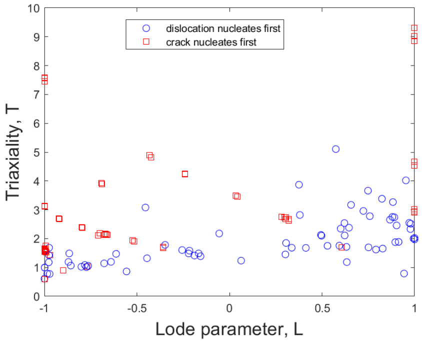

Figure 5: Relationship between triaxiality, T, and Lode parameter, L, from all of our simulations at the time of crack nucleation.

3.2. Critical stress for nucleation

Next, we further analyze our simulation results to better understand the critical conditions for void nucleation. An important feature of our simulations is that in many cases we observed void nucleation in the absence of plasticity (crack nucleation before dislocation nucleation). This enables us to first examine conditions for nucleation in the absence of plasticity, and then assess the influence of plasticity. Towards these goals, we compute the following global stress quantities at the time of crack nucleation, which define the critical conditions for nucleation: critical hydrostatic stress Σ_c^H, critical von Mises stress Σ_c^{vM}, critical maximum tensile stress Σ_c, and critical maximum shear stress τ_c. The maximum tensile and shear stresses were obtained using the principle stresses. An example showing how the critical hydrostatic stress was obtained is given in Figure 6(a). We also extracted the critical equivalent plastic strain ϵ_c^p, defined as the accumulated equivalent plastic strain between the time of dislocation nucleation and crack nucleation, as shown in Figure 6(b). Below, we report the most important features of these data (rather than reporting all of the data) in terms of explaining the critical conditions associated with void nucleation.

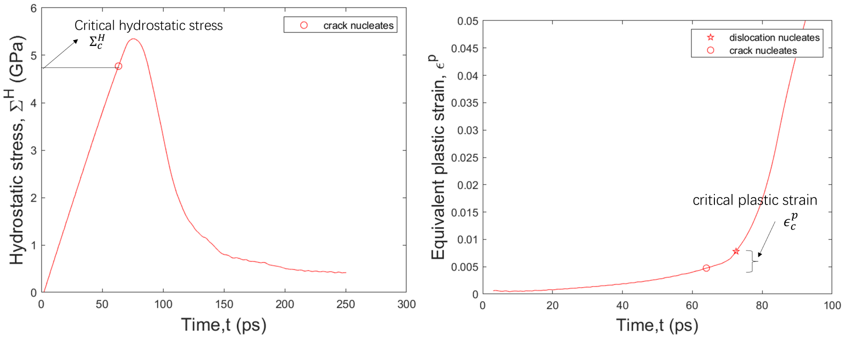

(a) (b)

Figure 6: Example results for $\omega_{xy} = \omega_{zx} = 1°$ showing how the critical values of (a) hydrostatic stress Σ_c^H and (b) equivalent plastic strain ϵ_c^p are obtained at the time of crack nucleation.

Since nearly all implementations of the GTN model use plastic strain as the driving force for nucleation, we begin by analyzing the critical plastic strain. Figure 7 shows how the critical plastic strain varies with (a) T and (b) L. Of course these results only include cases with plasticity prior to crack nucleation (dislocation nucleation and subsequent motion). The figure shows that the critical plastic strain varies widely from 0 up to about 0.25. Furthermore, there is essentially no correlation between the critical plastic strain and T or L. These results bring into question the notion of plastic strain as a driving force for nucleation. For example, based on existing models one might expect the critical plastic strain to take on a well-defined value at a particular T and L condition [15]. Our results are not consistent with this idea.

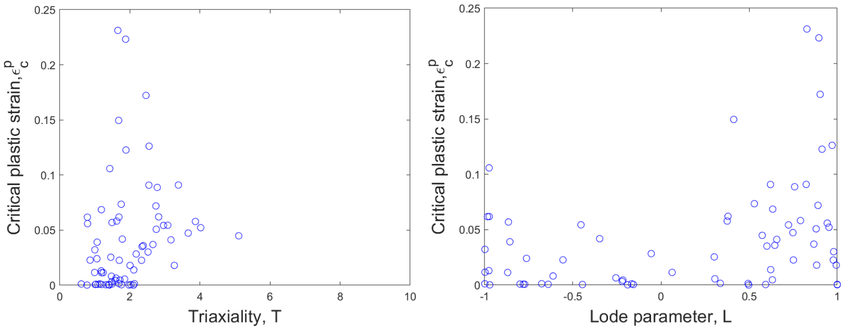

(a) (b)

Figure 7: Critical plastic strain as a function of (a) triaxiality T and (b) Lode parameter L.

Next, we consider how the critical stresses Σ_c^H and Σ_c depend on the triaxiality T and Lode parameter L, as shown in Figure 8. Again, in these figures we distinguish cases where plasticity occurs prior to void nucleation (blue circles) from cases where there is no plasticity prior to nucleation (red squares). Based on the discussion in the Introduction, we may expect that void nucleation occurs when a critical stress level is reached. Figure 8(a), shows how the critical hydrostatic stress varies with triaxiality. At very high triaxialities $T > 5$, void nucleation in the absence of plasticity seems to occur when a critical hydrostatic stress of 7 GPa is reached. However, at lower triaxialities the critical hydrostatic stress decreases below this value. Furthermore, there is no trend between the critical hydrostatic stress and the Lode parameter, as shown in Fig. 8(c). This indicates that the hydrostatic stress alone is not what drives void nucleation in the absence of plasticity.

On the other hand, the critical maximum tensile stress without plasticity shown in Figure 8(b) is relatively constant around 7 GPa for $T > 2$. This indicates that the critical tensile stress may be a good predictor for the onset of nucleation without plasticity. However, for low triaxialities the critical normal stress decreases below 7 GPa. The Lode parameter does not seem to be related to this behavior, since Figure 8(d) shows no relationship to L. To explain this behavior, we must account for the fact that the local normal stress σ is higher than the global stress Σ due to the elastic stress concentration at the particle's surface. Fig. 9(a) shows how the elastic stress concentration factor, as computed using finite element calculations, varies with triaxiality. A fit line of the form

$$\kappa^e = \frac{0.2584}{T^{0.4469}} + 1; \tag{13}$$

is shown to capture all stress states quite accurately, demonstrating that the local normal stress increases as T decreases. Using these stress concentration factors, we can obtain the local critical normal stress values $\sigma_c = \kappa^e \Sigma_c$ for cases without plasticity, and this is shown in Fig. 9(b). In this case, all simulation results collapse together quite well around an average critical local normal stress of $\sigma_c = 8.14$ GPa. This indicates that in the absence of plasticity it is the local maximum normal stress which controls void nucleation.

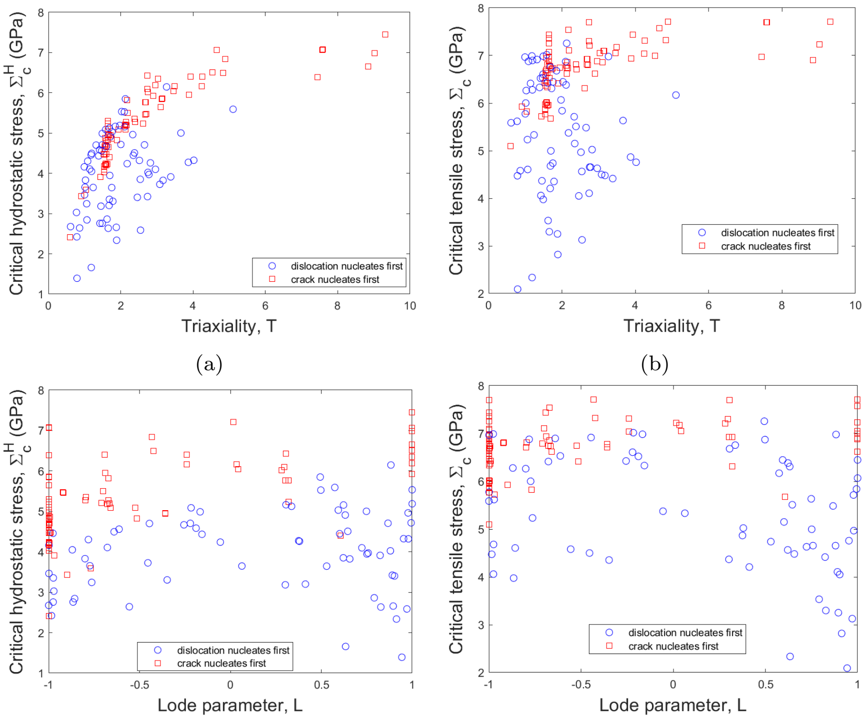

(a) (b)

(c) (d)

Figure 8: Critical global hydrostatic stress Σ_c^H (a,c) and (b,d) tensile stress Σ_c as a function of (a,b) triaxiality T and (c,d) Lode parameter L.

3.3. Influence of plasticity

While the analysis above explicates the nature of void nucleation without plasticity, when plasticity occurs prior to void nucleation the story is not so

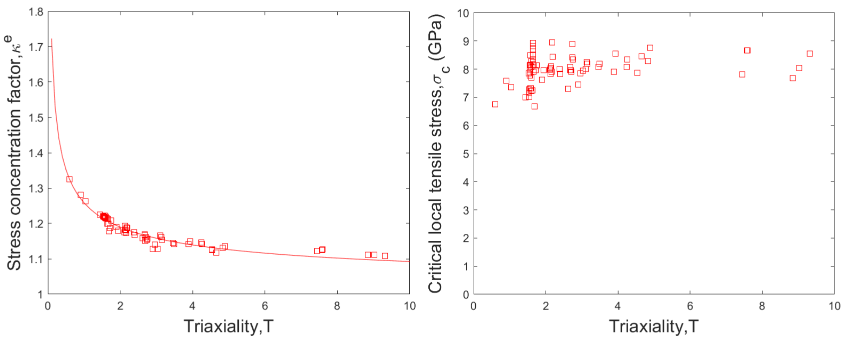

(a) (b)

Figure 9: (a) Elastic stress concentration factors obtained from finite element calculations for all simulations without plasticity. (b) Critical local tensile stress σ_c obtained from these stress concentration factors (only showing results where crack nucleation occurs first).

simple. Fig. 8(b) shows that in cases where dislocation nucleation precedes void nucleation (blue circles), the critical stresses can be significantly lower, as low as 2 GPa tensile stress. There is considerable scatter among the data with plasticity when plotting the critical stresses as a function of both T and L. This indicates that the applied stress state by itself cannot predict void nucleation in the presence of plasticity.

To investigate what gives rise to this behavior, we have analyzed the atomic plastic strains and stresses; example results of this analysis are shown in Fig. 10, with each row of images corresponding to a different simulation. These examples span triaxialities from $T = 0.2$ to 4 and Lode parameters from $L = -0.9$ to 0.9. The leftmost column of images shows where void nucleation occurs in each case, as indicated by the clusters of red atoms. The middle and rightmost columns show the states of equivalent plastic strain and radial normal stress, respectively, just before crack nucleation. In both cases, the fields are highly nonuniform; this non-uniformity derives from the plastic strain and dislocation distributions surrounding the particle. In all cases, the crack nucleation site is associated with a local hot spot of normal stress, whereas equivalent plastic strain does not always correlate with the nucleation site. Through manual analysis of our simulation results, we have confirmed that in the vast majority of cases the void nucleation site is associated with a region of local elevated normal stress. This analysis indicates that the sensitivity of the critical maximum tensile stress to plasticity is due to elevated local stresses at the particle interface, resulting from dislocation content and heterogeneous plastic strain.

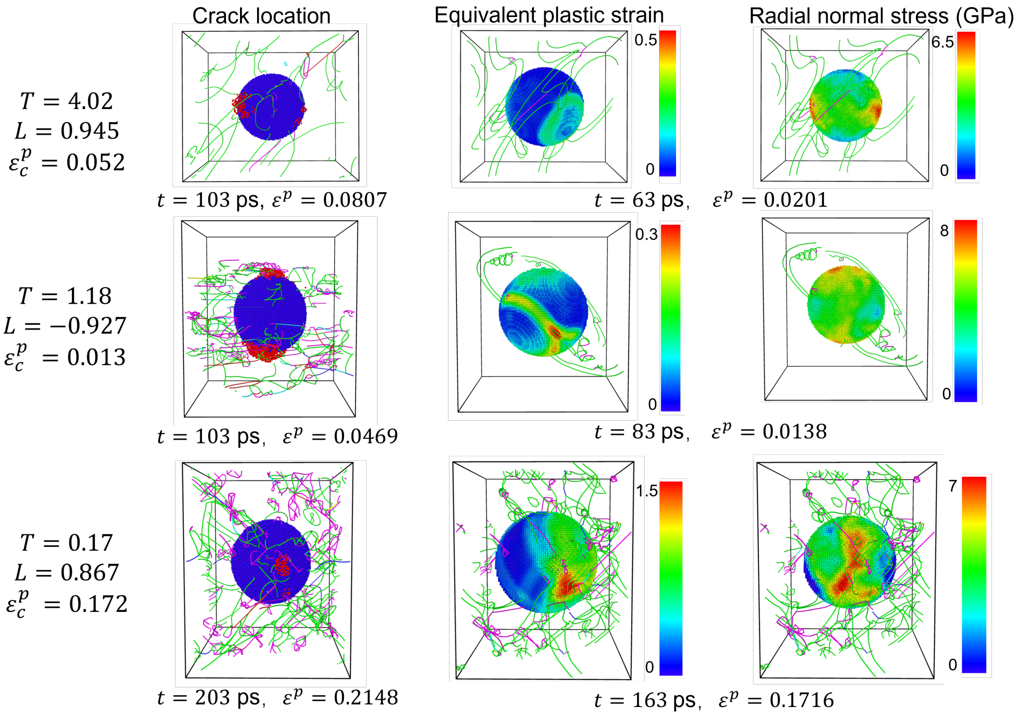

Figure 10: Example simulation snapshots showing (left) location of crack nucleation (red atoms), (middle) atomic equivalent plastic strain, and (right) atomic radial normal stress. Each row corresponds to a different simulation with nucleation conditions T, L, and ϵ_c^p given to the left.

As mentioned in the Introduction, two possible effects can contribute to the build up of local stresses at the particle interface: dislocation stress fields and plastic deformation. Even without any plastic deformation (i.e., no dislocation motion), the stress fields produced by dislocation lines near the interface will act on the interface, possibly elevated the stresses there. Furthermore, when dislocations intersect the particle interface, the disorder of the dislocation core may act to weaken the interface. Of note, however, is that none of the nucleation sites/normal stress hot spots in Fig. 10 are associated with a locally elevated density of dislocations. Again, through manual analysis we conclude that this is a general trend. To gain further insight into the potential role of dislocation content, we have extracted the total dislocation density at crack nucleation, ρ_c. Fig. 11(a) plots the critical tensile stress as a function of ρ_c; no clear trend is exhibited. These results lead us to conclude that the dislocation lines themselves are not strong contributors to void nucleation.

Once dislocations begin moving, they generate bands of local plastic strain in the Al matrix. However the particle, being incoherent and intermetallic, does not plastically deform. As a result, incompatibility stresses build up, as the matrix tries to change its shape but the particle resists this change. This idea is shown schematically in Fig. 12. To estimate the magnitude of this effect, we invoke the concept of a *plastic stress concentration factor* κ^p, which captures the stress amplification resulting from plastic deformation. Accordingly, we may write the nucleation criterion as

$$\sigma_c = \kappa^p \kappa^e \Sigma_c. \tag{14}$$

To estimate κ^p on the basis of our results, we assume that the true local critical normal stress for all simulations (including those with plasticity) is $\sigma_c = 8.14$ GPa. Accordingly, we can compute κ^p for each simulation as $\kappa_i^p = (8.14 \text{ GPa})/\kappa_i^e \Sigma_{c,i}$ where κ_i^e and $\Sigma_{c,i}$ and the elastic stress concentration factor and critical tensile stress for simulation i. The results are shown in Fig. 11(b). The plastic stress concentration factor is show to increase monotonically with plastic strain up to a value of about 2 when $\epsilon^p \approx 0.1$, albeit with a fair amount of scatter. This scatter is likely a direct consequence of the stochastic nature of plastic flow; the slip distribution from each simulation is a manifestation of random dislocation nucleation and glide events.

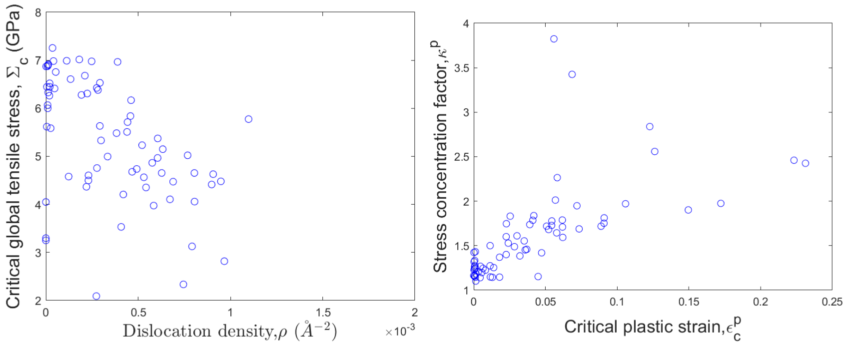

(a)

(b)

Figure 11: Effect of plasticity on critical stress for crack nucleation. (a) Critical maximum global tensile stress as a function of total dislocation density. (b) Plastic stress concentration factor as a function of equivalent plastic strain.

4. Discussion

A major finding of this work is that void nucleation by particle debonding is fundamentally a stress-driven phenomenon. For the Al-Cu system studied here, in the absence of plasticity a single critical local normal stress value 8.14 GPa is sufficient to predict void nucleation over a range of loading conditions (combinations of T and L). As far as we can tell, this critical stress is a property of the interface and not dictated by weak spots or defects in the interface (in our prior work we found no preferential nucleation sites under hydrostatic loading [20]). Introduction of additional defects such as vacancies may affect the critical stress, however. Hence, to predict nucleation all one needs to do is understand how stress is concentrated at the particle's surface, quantified by the elastic stress concentration factor κ^e. Interestingly, when we apply Argon et al.'s criterion Eq. (1) to our data we find that it also predicts nucleation with similar accuracy (e.g., the data collapse together around a single critical stress value, as in Fig. 9(b)). Of course this means that Needleman's criterion Eq. (2) is not consistent with our data. Note that to our knowledge, this is the first evidence that a stress-based nucleation criterion is valid all the way down to the nanoscale; previously it had been argued that stress-based criteria would only be valid for particles larger than about 1 μm [2], compared to our 10 nm particles here.

This local critical stress of approximately 8.14 GPa may appear exceedingly high from a macroscale perspective, since aluminum alloys typically have ultimate strengths around 500 MPa. However, two important factors make this number and its meaning more reasonable. Firstly, we show that plastic deformation can greatly reduce the critical global stress at which the critical local stress is reached. For example, Fig. 8 shows critical global stresses as low as 2 GPa. And secondly, the critical local stress is the stress that must be reached to nucleate an interface crack *in the absence of thermal activation*. Previous research [32, 33] and our own study in a companion paper [34] has shown that crack nucleation is a thermally activated process, meaning that at finite temperature cracks are able to nucleate at stresses below the critical stress. Our preliminary analysis for the same system used here indicates that at stresses around 500 MPa, cracks could nucleate on second timescales at room temperature; we plan to further detail this analysis in a future study.

When the matrix deforms plastically, the picture is rendered more complex but still largely explicable in terms of an additional stress concentration resulting from the plastic deformation, which we call κ^p here. This picture is, of course, completely consistent with the work of Lee and Mear [13], who showed that the stress concentration factor was plastic strain dependent. However our results here differ significantly from those of Lee and Mear in that our stress concentration factors are significantly larger. To compare with their results, we must estimate the modulus mismatch for our system, defined in terms of the ratio E'/E where E' is the Young's modulus of the particle and E is the modulus of the matrix. If we take the inverse of elements of the compliance tensor S_{11}^{-1}, S_{22}^{-1}, and S_{33}^{-1} as the effective Young's moduli for our anisotropic system here, we obtain modulus ratios between θ and Al in the range 1.8–2.7. Hence, we compare with results from Lee and Mear with a modulus ratio of $E'/E = 2$.

For spherical particles under uniaxial loading with $E'/E = 2$, Lee and Mear obtained a stress concentration at zero plastic strain of $\kappa^e = \kappa(\epsilon^p = 0) = 1.32$. At a plastic strain of $\epsilon^p = 0.05$, the stress concentration asymptotes to a value of $\kappa = 1.42$, giving a plastic stress concentration of $\kappa^p = \kappa/\kappa^e = 1.08$. Comparing with our results here in Fig. 11(b) where we obtain $\kappa^p \approx 1.5$ on average when $\epsilon^p = 0.05$, we conclude that our plastic stress concentrations are significantly larger. Furthermore, κ^p continues increasing out to a value of about 2 at a strain of $\epsilon^p = 0.1$. Beyond this strain level there is some evidence of an asymptote, but the data are sparse so it is difficult to judge. In addition, for load cases with higher triaxialities, Lee and Mear obtained that the stress concentration *decreases* with plastic strain, meaning $\kappa^p < 1$. This is in manifest disagreement with our results, where we observe that κ increases with plastic strain for all simulations. Hence we find significant qualitative and quantitative disagreement with Lee and Mear. Ironically, the approximate analysis of Beremin leading to Eq. (3) is in stronger agreement with our results, concluding that the stress concentration should roughly increase linearly with plastic strain. We see a similar trend in our data in Fig. 11, albeit with considerable scatter.

Why do our results disagree so significantly with the work of Lee and Mear? We believe the cause is the local homogenization of stress and strain fields in continuum theory. At the scale of crystal plasticity, discrete dislocation slip events impinge on the particle's interface. This leads to a highly fluctuating plastic strain field at the surface of the particle, thereby inducing a highly fluctuating stress field. When treated at the continuum scale, these fluctuations are completely suppressed because the local spatial averages of stress and plastic strain are the focus. Fig. 12 shows this idea qualitatively.

But crack nucleation is driven by the maximum value of the local stress, not the average value. In other words, continuum theory homogenizes away the most critical piece of information for understanding the propensity for void nucleation. This is thus an example where continuum theory is not an ideal tool for studying behaviors of materials.

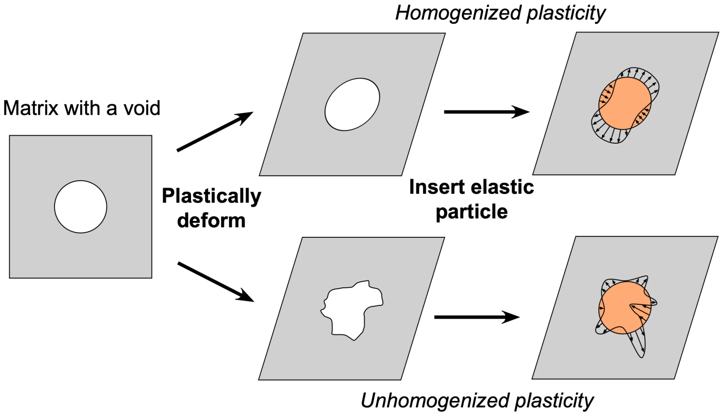

Figure 12: Schematic showing the stress field at the matrix-particle interface (top) with homogenized plasticity (continuum theory) and (bottom) with unhomogenized plasticity (MD). Unhomogenized plasticity leads to localized hot spots of stress.

Of course we must take care in our analysis here since our simulation strain rates are significantly elevated relative to quasi-static loading. However, we believe that these elevated strain rates do not influence our results too significantly. The major effects of dynamic loading are (1) formation and propagation of transient stress waves that induce local stress fluctuations and (2) rate-dependent evolution of the dislocation structure. In regards to (1), we did not see evidence that transient stress waves had much effect on the stress states. For example, we observed consistent evolution of local stress states over time without strong fluctuations expected if transient waves were dominant. None-the-less, future efforts should more carefully determine the sensitivity to strain rate. In regards to (2), there is likely some influence of strain rate on the plastic-strain-dependence of void nucleation. However, this sensitivity is difficult to assess via MD simulations alone, since the range of accessible strain rates is rather narrow. Additional modeling techniques such as discrete dislocation dynamics [35] likely need to be employed to understand this rate effect over a broader, and more relevant, strain rate range.

One subtle aspect of our analysis here is the definition of "void nucleation". We have focused on the moment at which an interface crack appears. However in order for a "void" to nucleate, this interface crack must propagate along the interface some amount until the void is able to start growing plastically rather than via further debonding. Needleman [3] instead defined nucleation as the point at which the particle has sufficiently debonded to behave asymptotically like a void (i.e., at large strains), and this definition is the basis for Eq. (2). This may explain differences between Needleman's analysis and ours here. In our prior work we quantified the rate of debonding in detail and found that dislocation activity significantly accelerates the rate of interfacial crack growth [20]. Additional research is necessary to identify the best definition of "void nucleation" in terms of most clearly understanding ductile fracture.

We conclude by commenting on the implications of our results for ductile fracture modeling. The most popular approach uses GTN with plastic deformation as the driving force v for the nucleation. As emphasized by Noell et al., this approach is not consistent with the physics of void nucleation, and our results here are in agreement with this point. While plastic deformation has a strong effect on nucleation, it is not predictive by itself. Instead, one must consider both the stress state and the state of plastic strain. An important question related to this problem is: what feature of the plastic strain state is most informative for predicting nucleation? While Fig. 11(b) has a fair amount of scatter, the overall trend is strong and clear. This gives evidence that equivalent plastic strain ϵ^p is a sufficient quantitative metric of plastic deformation for void nucleation models. Furthermore, our simulations here spanned a large range of triaxialities and Lode parameters (perhaps the most expansive study to date). Of course, we have only considered one material system and one particle geometry, so the story may be more complicated in other circumstances. None-the-less, our results here suggest that future research efforts should be aimed at re-integrating stress in conjunction with plastic strain into the nucleation term for ductile fracture models, such as was originally developed by Needleman, Tvergaard, and colleagues [36, 37].

5. Conclusion

We have employed MD simulations to identify the critical conditions for the initiation of void nucleation via particle delamination in Al containing a θ-particle. With this objective, we performed hundreds of MD simulations with varying stress states, as quantitifed by the stress triaxiality and Lode parameter. For high triaxiality simulations, we observed that an interface crack nucleated before any dislocations nucleated, making void nucleation an entirely elastic phenomenon. Through analysis of these simulations we demonstrated that, to a good approximation, nucleation occurs when a critical local normal stress of 8.14 GPa is reached at the particle surface. With lower triaxialities, dislocation nucleation preceded crack nucleation, causing plastic strain to be produced prior to void nucleation. In these simulations, the equivalent plastic strain by itself could not predict when nucleation would occur. Instead, by leveraging our results without dislocation nucleation we were able to infer a plastic stress concentration factor κ^p, which resulted from the plastic strain distribution surrounding the particle. When analyzed in this way, a linear trend was recovered between the plastic stress concentration factor and the equivalent plastic strain. The influence of plastic strain implied by our results was found to be significantly greater than that obtained by Lee and Mear with continuum plasticity calculations. We interpret this difference in terms of the influence of plastic strain homogenization on the local stress field at the matrix-particle interface. Such homogenization eliminates hot spots of stress which drive nucleation.

To our knowledge this work provides the first atomistic study of void nucleation which critically assesses the conditions associated with void nucleation. Of course given the length and time scale constraints of MD, our simulation conditions are significantly different from those observed in experimental observations of ductile fracture (e.g., micron-scale particles loaded to 100s of MPa). None-the-less, we believe that our results here provide insights which extend beyond the limitations of the simulations, enabling an understanding of void nucleation which can inform experimental contexts. Additional research is needed to asses the influence of other key variables on nucleation, such as particle size, shape, matrix crystal structure, and temperature.

Acknowledgements

The authors thank Heather Schein for assisting with simulation analysis. This material is based upon work supported by the National Science Foundation under Grant No. CMMI-2034074.

Data statement

All data presented herein are available at the following data DOI: 10.5281/zenodo.10806843

References

[1] A. Pineau, A. Benzerga, T. Pardoen, Failure of metals I: Brittle and ductile fracture, Acta Materialia 107 (2016) 424–483. doi:10.1016/j.actamat.2015.12.034.

[2] P. J. Noell, R. B. Sills, A. A. Benzerga, B. L. Boyce, Void nucleation during ductile rupture of metals: A review, Progress in Materials Science 135 (2023) 101085. doi:10.1016/j.pmatsci.2023.101085.

[3] A. Needleman, A Continuum Model for Void Nucleation by Inclusion Debonding, Journal of Applied Mechanics 54 (3) (1987) 525–531. doi:10.1115/1.3173064.

[4] M. N. Shabrov, A. Needleman, An analysis of inclusion morphology effects on void nucleation, Modelling and Simulation in Materials Science and Engineering 10 (2) (2002) 163–183. doi:10.1088/0965-0393/10/2/305.

[5] J. Besson, Continuum Models of Ductile Fracture: A Review, International Journal of Damage Mechanics 19 (1) (2010) 3–52. doi:10.1177/1056789509103482.

[6] M. Shakoor, V. M. Trejo Navas, D. Pino Munõz, M. Bernacki, P.-O. Bouchard, Computational Methods for Ductile Fracture Modeling at the Microscale, Archives of Computational Methods in Engineering 26 (4) (2019) 1153–1192. doi:10.1007/s11831-018-9276-1.

[7] K. Tanaka, T. Mori, T. Nakamura, Cavity formation at the interface of a spherical inclusion in a plastically deformed matrix, The Philosophical Magazine: A Journal of Theoretical Experimental and Applied Physics 21 (170) (1970) 267–279. doi:10.1080/14786437008238415.

[8] A. Argon, J. Im, R. Safoglu, Cavity formation from inclusions in ductile fracture, Metallurgical transactions A 6 (1975) 825–837.

[9] S. Goods, L. Brown, Overview No. 1, Acta Metallurgica 27 (1) (1979) 1–15. doi:10.1016/0001-6160(79)90051-8.

[10] J. Segurado, J. LLorca, A new three-dimensional interface finite element to simulate fracture in composites, International journal of solids and structures 41 (11-12) (2004) 2977–2993.

[11] J. Williams, J. Segurado, J. LLorca, N. Chawla, Three dimensional (3D) microstructure-based modeling of interfacial decohesion in particle reinforced metal matrix composites, Materials Science and Engineering: A 557 (2012) 113–118. doi:10.1016/j.msea.2012.05.108.

[12] F. M. Beremin, Cavity formation from inclusions in ductile fracture of A508 steel, Metallurgical Transactions A 12 (5) (1981) 723–731. doi:10.1007/BF02648336.

[13] B. Lee, M. Mear, Stress concentration induced by an elastic spheroidal particle in a plastically deforming solid, Journal of the Mechanics and Physics of Solids 47 (6) (1999) 1301–1336. doi:10.1016/S0022-5096(98)00104-5.

[14] Y. Charles, R. Estevez, Y. Bréchet, E. Maire, Modelling the competition between interface debonding and particle fracture using a plastic strain dependent cohesive zone, Engineering Fracture Mechanics 77 (4) (2010) 705–718. doi:10.1016/j.engfracmech.2009.11.012.

[15] G. Testa, N. Bonora, A. Ruggiero, G. Iannitti, D. Gentile, Stress triaxiality effect on void nucleation in ductile metals, Fatigue & Fracture of Engineering Materials & Structures 43 (7) (2020) 1473–1486. doi:10.1111/ffe.13212.

[16] A. L. Gurson, Continuum Theory of Ductile Rupture by Void Nucleation and Growth: Part I—Yield Criteria and Flow Rules for Porous Ductile Media, Journal of Engineering Materials and Technology 99 (1) (1977) 2–15. doi:10.1115/1.3443401.

[17] V. Tvergaard, A. Needleman, Analysis of the cup-cone fracture in a round tensile bar, Acta Metallurgica 32 (1) (1984) 157–169. doi:10.1016/0001-6160(84)90213-X.

[18] J. Koplik, A. Needleman, Void growth and coalescence in porous plastic solids, International Journal of Solids and Structures 24 (8) (1988) 835–853. doi:10.1016/0020-7683(88)90051-0.

[19] M. Kuna, D. Z. Sun, Three-dimensional cell model analyses of void growth in ductile materials, International Journal of Fracture 81 (3) (1996) 235–258. doi:10.1007/BF00039573.

[20] Q. Q. Zhao, B. L. Boyce, R. B. Sills, Micromechanics of Void Nucleation and Early Growth at Incoherent Precipitates: Lattice-Trapped and Dislocation-Mediated Delamination Modes, Crystals 11 (1) (2021) 45. doi:10.3390/cryst11010045.

[21] J.-F. Nie, 20 Physical Metallurgy of Light Alloys, in: D. E. Laughlin, K. Hono (Eds.), Physical Metallurgy, 2014, pp. 2009–2156.

[22] B. Wisner, A. Kontsos, Investigation of particle fracture during fatigue of aluminum 2024, International Journal of Fatigue 111 (2018) 33–43. doi:10.1016/j.ijfatigue.2018.02.001.

[23] W. Cai, J. Li, S. Yip, Molecular Dynamics, in: Comprehensive Nuclear Materials, Elsevier, 2012, pp. 249–265. doi:10.1016/B978-0-08-056033-5.00128-2.

[24] A. P. Thompson, H. M. Aktulga, R. Berger, D. S. Bolintineanu, W. M. Brown, P. S. Crozier, P. J. in 't Veld, A. Kohlmeyer, S. G. Moore, T. D. Nguyen, R. Shan, M. J. Stevens, J. Tranchida, C. Trott, S. J. Plimpton, LAMMPS - a flexible simulation tool for particle-based materials modeling at the atomic, meso, and continuum scales, Computer Physics Communications 271 (2022) 108171. doi:10.1016/j.cpc.2021.108171.

[25] F. Apostol, Y. Mishin, Interatomic potential for the Al-Cu system, Physical Review B 83 (5) (2011) 054116. doi:10.1103/PhysRevB.83.054116.

[26] A. Stukowski, Visualization and analysis of atomistic simulation data with OVITO–the Open Visualization Tool, Modelling and Simulation in Materials Science and Engineering 18 (1) (2010) 015012. doi:10.1088/0965-0393/18/1/015012.

[27] A. Stukowski, Structure identification methods for atomistic simulations of crystalline materials, Modelling and Simulation in Materials Science and Engineering 20 (4) (2012) 045021. doi:10.1088/0965-0393/20/4/045021.

[28] A. Stukowski, K. Albe, Extracting dislocations and non-dislocation crystal defects from atomistic simulation data, Modelling and Simulation in Materials Science and Engineering 18 (8) (2010) 085001. doi:10.1088/0965-0393/18/8/085001.

[29] P. S. Branicio, D. J. Srolovitz, Local stress calculation in simulations of multicomponent systems, Journal of Computational Physics 228 (22) (2009) 8467–8479. doi:10.1016/j.jcp.2009.08.024.

[30] A. P. Thompson, S. J. Plimpton, W. Mattson, General formulation of pressure and stress tensor for arbitrary many-body interaction potentials under periodic boundary conditions, The Journal of Chemical Physics 131 (15) (2009) 154107. doi:10.1063/1.3245303.

[31] Y. Mishin, D. Farkas, M. J. Mehl, D. A. Papaconstantopoulos, Interatomic potentials for monoatomic metals from experimental data and *ab initio* calculations, Physical Review B 59 (5) (1999) 3393–3407. doi:10.1103/PhysRevB.59.3393.

[32] V. Berdichevsky, K. C. Le, On The Microcrack Nucleation In Brittle Solids, International Journal of Fracture 133 (4) (2005) L47–L54. doi:10.1007/s10704-005-0632-4.

[33] C. L. Dias, J. Kröger, D. Vernon, M. Grant, Nucleation of cracks in a brittle sheet, Physical Review E 80 (6) (2009) 066109. doi:10.1103/PhysRevE.80.066109.

[34] Y. Fang, Q. Q. Zhao, R. B. Sills, A. A. Ezzat, Constructing coarse-grained models with physics-guided gaussian process regression, In-Preparation.

[35] R. B. Sills, W. P. Kuykendall, A. Aghaei, W. Cai, Fundamentals of Dislocation Dynamics Simulations, in: C. R. Weinberger, G. J. Tucker (Eds.), Multiscale Materials Modeling for Nanomechanics, Vol. 245, Springer International Publishing, Cham, 2016, pp. 53–87.

[36] C. C. Chu, A. Needleman, Void Nucleation Effects in Biaxially Stretched Sheets, Journal of Engineering Materials and Technology 102 (3) (1980) 249–256. doi:10.1115/1.3224807.

[37] V. Tvergaard, A. Needleman, The Modified Gurson Model, in: Handbook of Materials Behavior Models, Elsevier, 2001, pp. 430–435. doi:10.1016/B978-012443341-0/50048-X.